

Ion Migration-Induced Amorphization and Phase Segregation as a Degradation Mechanism in Planar Perovskite Solar Cells

Diego Di Girolamo, Nga Phung, Felix Utama Kosasih, Francesco Di Giacomo, Fabio Matteocci, Joel A. Smith, Marion A. Flatken, Hans Köbler, Silver H. Turren Cruz, Alessandro Mattoni, Lucio Cinà, Bernd Rech, Alessandro Latini, Giorgio Divitini, Caterina Ducati, Aldo Di Carlo,* Danilo Dini,* and Antonio Abate*

The operation of halide perovskite optoelectronic devices, including solar cells and LEDs, is strongly influenced by the mobility of ions comprising the crystal structure. This peculiarity is particularly true when considering the long-term stability of devices. A detailed understanding of the ion migration-driven degradation pathways is critical to design effective stabilization strategies. Nonetheless, despite substantial research in this first decade of perovskite photovoltaics, the long-term effects of ion migration remain elusive due to the complex chemistry of lead halide perovskites. By linking materials chemistry to device optoelectronics, this study highlights that electrical bias-induced perovskite amorphization and phase segregation is a crucial degradation mechanism in planar mixed halide perovskite solar cells. Depending on the biasing potential and the injected charge, halide segregation occurs, forming crystalline iodide-rich domains, which govern light emission and participate in light absorption and photocurrent generation. Additionally, the loss of crystallinity limits charge collection efficiency and eventually degrades the device performance.


1. Introduction

Metal halide perovskites have achieved extraordinary results as a photovoltaic (PV) material and have recently surpassed 25% in certified power conversion efficiency (PCE) since the first demonstration in 2009.^[1,2] This outstanding achievement is made possible by advantageous optoelectronic properties of perovskites, including long charge carrier diffusion length^[3] and steep light absorption onset.^[4] The common stoichiometry for the perovskite structure is ABX_3 , where A is a monovalent cation (e.g., methylammonium (MA^+), formamidinium (FA^+), or cesium (Cs^+)), B is a divalent cation (commonly Pb^{2+} or Sn^{2+}), and X is a halide. Tuning the perovskite composition of this class of materials varies their band gaps.^[5,6] Hence, halide perovskites can be a suitable absorber

Dr. D. Di Girolamo, Dr. A. Latini, Prof. D. Dini
Department of Chemistry
University of Rome "Sapienza"
Piazzale Aldo Moro 5, Rome 00185, Italy
E-mail: danilo.dini@uniroma1.it

Dr. D. Di Girolamo, Dr. A. Abate
Department of Chemical
Materials and Production Engineering
University of Naples Federico II
Piazzale Tecchio 80, Fuorigrotta, Naples 80125, Italy
E-mail: antonio.abate@helmholtz-berlin.de, antonio.abate@unina.it

N. Phung, M. A. Flatken, H. Köbler, Dr. S. H. Turren Cruz,
Prof. B. Rech, Dr. A. Abate
Department of Renewable Energy
Helmholtz-Zentrum Berlin für Materialien und Energie
Kekuléstraße 5, Berlin 12489, Germany

 The ORCID identification number(s) for the author(s) of this article can be found under <https://doi.org/10.1002/aenm.202000310>.

© 2020 The Authors. Published by WILEY-VCH Verlag GmbH & Co. KGaA, Weinheim. This is an open access article under the terms of the Creative Commons Attribution License, which permits use, distribution and reproduction in any medium, provided the original work is properly cited.

DOI: 10.1002/aenm.202000310

F. U. Kosasih, Dr. G. Divitini, Prof. C. Ducati
Department of Materials Science and Metallurgy
University of Cambridge
27 Charles Babbage Road, Cambridge CB3 0FS, UK
Dr. F. Di Giacomo, Dr. F. Matteocci, Prof. A. Di Carlo
Centre for Hybrid and Organic Solar Energy (CHOSE)
Department of Electronic Engineering
University of Rome-Tor Vergata
Rome 00133, Italy
E-mail: aldo.dicarlo@uniroma2.it

J. A. Smith
Department of Physics and Astronomy
University of Sheffield
Sheffield S3 7RH, UK

Dr. A. Mattoni
Consiglio Nazionale delle Ricerche
Istituto Officina dei Materiali
CNR-IOM, Cagliari
Cittadella Universitaria
Monserrato, Cagliari 09042-1, Italy

Dr. L. Cinà
CICCI Research
Piazzale Thailandia, 5, Grosseto 58100, Italy

material for both single-junction and multi-junction solar cells.^[7] Notably, the facile deposition of hybrid perovskites offers an opportunity for incorporation with commercial PV technologies, such as silicon, in a tandem architecture.^[8] Further, compositional engineering has been a pivotal step to improve the efficiency and stability of perovskite solar cells (PSCs). This has enabled the adoption of FA-based perovskites, which have better thermal stability than methylammonium lead iodide (MAPbI₃).^[9–11] Saliba et al. introduced the “triple cation” perovskite with a Cs_{0.05}(FA_{0.83}MA_{0.17})_{0.95}Pb(I_{0.83}Br_{0.17})₃ stoichiometry, henceforth labeled CsFAMA, which is now a standard in the perovskite community.^[12]

Lead halide perovskites are mixed ionic-electronic conductors, and this has a profound impact on solar cell behavior. Hysteresis in current density–voltage (*J*–*V*) scans has been attributed at least partially to ion migration,^[13,14] which is broadly identified as one of the leading causes of PSCs’ instability,^[15] compromising the structural integrity of the perovskite film and the whole device.^[16–19] Together with ion migration, chemical and electrochemical^[20] interactions of perovskite constituent ions with the selective contacts^[21–23] and electrodes^[24–26] can degrade the devices. However, the detailed mechanisms behind ion migration-driven hysteresis and degradation remain elusive, due to the chemical complexity of perovskite systems and the coupling between electronic and ionic current, which renders experimental design challenges.

Applying an electrical bias to a solar cell is the most direct way to investigate ion-driven instabilities in a full device. For instance, in our previous work, we investigated hysteresis in the dark, which is linked to interface instability due to the interaction of perovskite with selective contacts.^[21] The importance of selective contacts on the electrical bias stability was further highlighted by an in situ transmission electron microscopy (TEM) investigation by Jung et al., who observed the migration of oxygen from TiO₂ to MAPbI₃ in forward bias.^[27] In a similar experiment, morphological and chemical degradation was observed at the 2,2',7,7'-tetrakis[*N,N*-di(4-methoxyphenyl)amino]-9,9'-spirobifluorene (spiro-OMETAD)/MAPbI₃ interface due to the interaction between iodide and spiro-OMETAD.^[28] Different studies reported the formation of PbI₂ as a degradation product due to biasing of MAPbI₃ films.^[29–32] However, most of these studies employed ad hoc devices (e.g., lateral devices), which are not entirely representative of standard solar cell architectures. Similarly, investigations on “half-cell” configurations are also unrepresentative, where both electrostrictive behavior of perovskite films^[33] and the formation of periodically striped ferroelastic domains have been observed with scanning probe microscopy.^[34] Similarly, Luchkin et al. showed changes in surface topography upon biasing the perovskite film.^[35] It remains to be seen whether the same phenomenon occurs in a full device, where both perovskite surfaces are covered with a selective contact and an electrode. Furthermore, upon biasing,

the devices are subjected to charge injection, which might induce unpredictable processes if only the ions’ drift-diffusion behavior is accounted for. In fact, there is clear evidence that a high concentration of charge carriers and interface electrochemistry drive halide segregation.^[36–38]

In this work, we investigated the effects of ion migration and charge injection by forward biasing planar p-i-n PSCs on a time-scale of hours, simulating to a certain extent the electrical load experienced during 1 day of PV operation. We aimed to advance the understanding of PSCs instabilities due to ionic conductivity by bridging the gap between the materials chemistry and the device performances and optoelectronics. Except for TEM, all characterizations were performed in situ, with the bias applying directly on the sample during the measurement to minimize (or avoid) the effects of relaxation, and thus, it was able to fully observe the consequences of electrical bias on the device.

Our findings suggest that the loss in mixed halide perovskite based solar cells performance is driven by a combination of halide segregation and perovskite amorphization, with the latter likely driven by defect accumulation at the interfaces. The iodide-rich crystalline domains govern the light emission and participate (inefficiently) in the generation of photocurrent. The charge collection is hindered by the amorphous phase, pointing to degradation at the interfaces between perovskite and charge selective layers.

2. Result and Discussion

In this study, we employed a planar p-i-n configuration consisting of glass/ITO/NiO/CsFAMA/C₆₀/BCP/Cu (Figure 1a). This device architecture has been promising to achieve long-term stability.^[39,40] The absence of hysteresis in p-i-n devices also simplified the analysis of the device behavior. With our fabrication procedure, detailed in the Experimental Section, we obtained devices with negligible hysteresis and PCEs approaching 18%, in line with NiO-based PSCs in literature.^[41–44] Statistics and reproducibility of PV parameters are reported in Figure S1, Supporting Information. In Figure 1b, we report the effect on *J*–*V* curves after 12 h of polarization at 1.2 V in the dark, in a condition similar to the novel ISOS-*V* protocols.^[45] In this condition, we were simulating/accelerating the effect of operating voltage on ion migration and at a current density similar to under PV operation (further discussion on this point is in Note 1, Supporting Information). This stress test considerably decreased the short circuit current (*J*_{SC}, from 21.1 to 16.5 mA cm^{−2}) and fill factor (FF, from 73% to 48%) of the device while increased the open-circuit voltage (*V*_{OC}) by 70 mV as can be seen in Figure 1b. Overall, the device efficiency was reduced by about 50% (relative), from 16% to 8% (absolute).

We noticed that, within the time frame of observation, the overlap with the electrical bias of light (Figure 1c) and thermal stress at 65 °C (Figure 1d) had similar effects on the *J*–*V* curve compared to only bias stress. This suggested a central role of the bias in the degradation of PSCs. Notably, the combination of higher temperature and bias severely increased the degradation rate. This implied that thermal and bias stress could be used in accelerating stability tests for this perovskite based solar cells. By stressing the cell at *V*_{OC} or in dark at 1 V, a similar effect on the *J*–*V* curve was obtained (Figure S2, Supporting Information). In agreement with previous reports, the increase in

Prof. B. Rech
Faculty of Electrical Engineering and Computer Science
Technical University Berlin
Marchstraße 23, Berlin 10587, Germany

Prof. A. Di Carlo
Laboratory of Advanced Solar Energy (LASE)
National University of Science and Technology NUST-MISiS
Leninskiy prospect 6, Moscow 119049, Russia

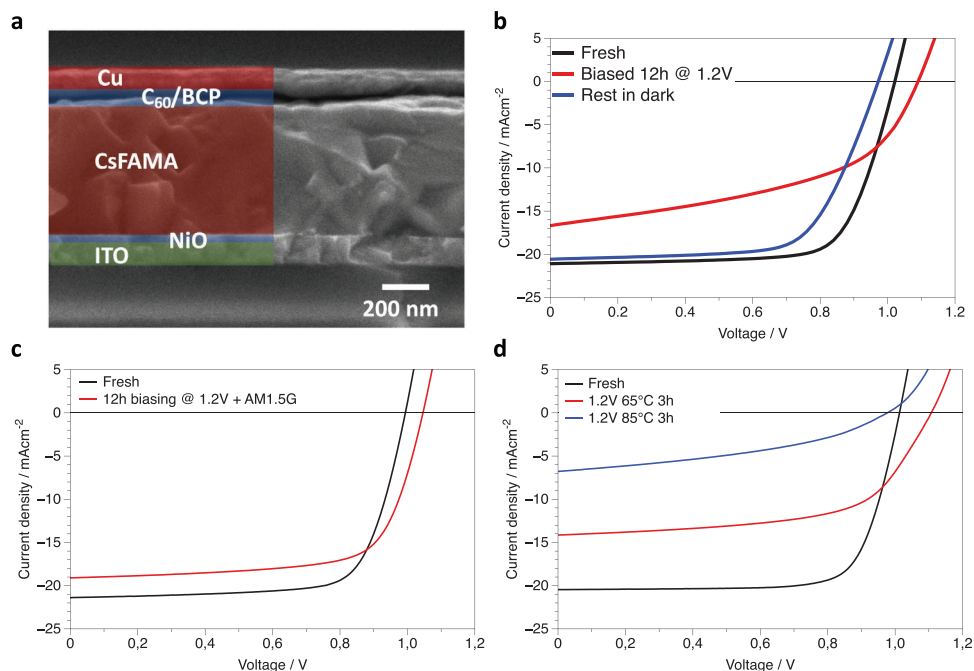


Figure 1. a) SEM cross section and architecture of the PSCs employed in this work. CsFAMA stands for the $\text{Cs}_{0.05}((\text{FAPbI}_3)_{0.83}(\text{MAPbBr}_3)_{0.17})_{0.95}$ perovskite composition. b) J - V curves of a fresh cell (black), after bias at 1.2 V in the dark for 12 h (red), and after rest in the dark for 6 h (blue). c) J - V curves of a fresh cell (black), after bias at 1.2 V under illumination AM 1.5 g for 12 h (red). d) J - V curves of a fresh cell (black), after bias at 1.2 V in the dark for 12 h at 65 °C (red) and 85 °C (blue).

V_{OC} could be explained considering the asymmetric self-doping of the perovskite layer arising from the redistribution of ionic defects upon poling.^[46–48] This might affect also the charge collection efficiency and thus the J_{SC} .^[46] It is important to note that the biased state was not stable, and after resting in the dark and in inert (N_2) atmosphere for 6 h, the FF and J_{SC} partially recovered their initial values and the V_{OC} stabilized below its initial value. This slow recovery from the biased state might partially stem from the gradual relaxation of ionic distribution induced by the bias, similarly to the case of reversible PCE losses over a day (stress)/night (recovery) cycling.^[15]

To gain an insight into the crystal quality of the perovskite layer during the stress test, we performed in situ X-ray diffraction (XRD) while biasing at 1.2 V in the dark. As detailed in the Experimental Section, only part of the sample surface was biased, thus quantitative analysis underestimated the observed phenomena. In **Figure 2a**, we show the comparison of the full XRD pattern of the fresh sample and after 12 h of biasing at 1.2 V in the dark. In **Figure 2b**, we show the decline of the integrated intensity of representative peaks (i.e., 12.7° for PbI_2 and 14.2° and 28.4° for perovskite) over the stressing time, which is proportional to the variation of the coherently diffracting domain of the pertaining crystalline phase.^[50,51] Interestingly, the PbI_2 XRD peak decreased by 40% (see also **Figure S4**, Supporting Information), suggesting that crystalline PbI_2 was not the degradation product of CsFAMA perovskite under the effect of bias, as in the case of MAPbI_3 .^[52]

Along with the reduction of crystalline PbI_2 , we observed a loss of perovskite crystallinity, with the reduction of scattering intensity around 10%, indicating a reduction in the long-range ordering of the structure and pointing towards amorphization. It is widely accepted that biasing a PSC leads to the formation

of ionic space charge at the interfaces of perovskite with selective contacts, which affects the doping profile and charge dynamics at the interfaces; this is considered the main reason for device J - V hysteresis.^[13,53,54] Our results show that in addition to the above effects, ion migration on a timescale comparable to daily PV operations induced the partial collapse of the perovskite structure. Molecular dynamics (MD) simulations on the model system $\text{CH}_3\text{NH}_3\text{PbI}_3$ confirmed that the perovskite lattice collapsed when an excessive defect density was accumulated (see **Figure S5**, Supporting Information). The asymmetric broadening of perovskite XRD peaks (representative 002 peak is magnified in **Figure 2c**) could be explained by either the introduction of inhomogeneous tensile strain^[55] or the appearance of new species with the same perovskite crystalline structure and a slightly larger unit cell. A synchrotron-based in situ grazing-incidence wide-angle X-ray scattering (GI-WAXS) experiment clarified that the evolution of the peak shape originated from peak splitting, as shown in **Figure 2d**. This result is similar to the findings by Andaji-Garmaroudi et al.^[56] and is a strong indicator of halide segregation,^[57] with the additional crystalline species reasonably being ascribed to an iodide-rich perovskite (see **Figure S7**, Supporting Information).

The devices were subjected to an electroluminescence (EL) measurement to confirm the presence of the iodide phase. As can be seen in **Figure 2e**, the appearance of iodide rich domains was evident from the evolution of the EL spectrum upon biasing, in agreement with the results from Ruf et al. employing the same CsFAMA stoichiometry as in this work.^[58] A low-band gap-emitting species was detected already after a few minutes, and it governs light emission after 3 h of biasing at 1.2 V. The EL peak of the 3 h biased-state stabilized at 790 nm (1.57 eV), a

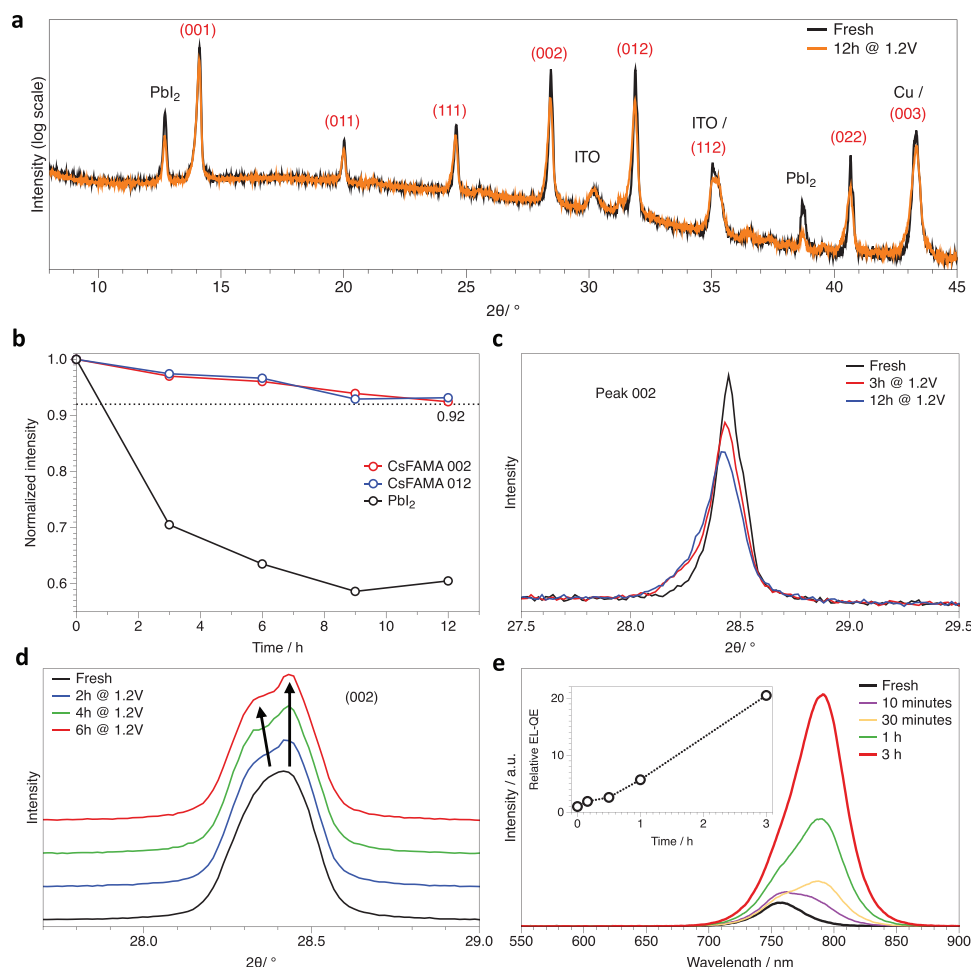


Figure 2. a) Comparison between the XRD patterns of the fresh sample (black) and collected after 12 h of continuous forward bias at 1.2 V (orange). The intensity is plotted on a logarithmic scale to highlight low-intensity peaks and to confirm that no crystalline phases are present other than Cu, ITO, Pbl₂, and perovskite. Indexing of XRD peaks from perovskite is depicted in red, taken from the study by Xie et al.^[49] There is an overlapping of perovskite peaks with ITO ($\approx 35^\circ$) and Cu ($\approx 43^\circ$), as explained in Figure S4, Supporting Information. b) Variation of the integrated intensity of selected peaks during biasing. c) Detail from (a) highlighting the peak associated with the (002) plane of the perovskite phase at $\approx 28.4^\circ$. d) Evolution of the perovskite peak at 28.4° , obtained from in situ GIWAXS measurements, showing peak splitting upon biasing at 1.2 V in the dark. The different spectra are shifted on the y-axis. e) Evolution of EL spectrum upon biasing the cell at 1.2 V in the dark. In the inset, the EL-QE is plotted relative to the fresh sample (EL – QE = 1), which increases by a factor of 20 after 3 h of biasing. A gradual transition of peak emission wavelength from 760 nm for the fresh sample to 790 nm after 3 h bias is observed.

30 nm red-shift from the pristine state's 760 nm peak (1.63 eV). The iodide-rich phase after 3 h biasing was not a pure iodide triple-cation perovskite ($\text{Cs}_{0.05}(\text{FA}_{0.83}\text{MA}_{0.17})_{0.95}\text{PbI}_3$), whose emission peak was located at 805 nm (1.54 eV, see Figure S8, Supporting Information). A putative halide ratio of this low-band gap-emitting species could be obtained by estimating a linear relation between the band gap and halide composition,^[7] which yielded an iodide percentage of 94%. The fairly stable EL peak position upon biasing of the $\text{Cs}_{0.05}(\text{FA}_{0.83}\text{MA}_{0.17})_{0.95}\text{PbI}_3$ perovskite (see Figure S8, Supporting Information) indicated to a minor or null role of A-site cation segregation in the formation of the narrow band gap perovskite.^[59] The increase of EL quantum efficiency (EL-QE) has been reported widely in the case of halide segregation.^[37,57] However, we also observed this effect with $\text{Cs}_{0.05}(\text{FA}_{0.83}\text{MA}_{0.17})_{0.95}\text{PbI}_3$ and MAPbI₃ (Figure S8, Supporting Information), despite a constant EL peak position. This suggested a possible convolution of different processes

rather than only halide segregation causing the increase in EL-QE. The evolution of optoelectronic properties of halide perovskite in timescales of seconds to minutes could be rationalized through ion migration-induced defect formation or annihilation,^[60–63] and similar argument could be used to explain the increment of EL-QE.

The anti-correlation found between V_{OC} and crystallinity after biasing was intriguing and unexpected. In fact, Tsai et al. reported that the increased V_{OC} (and FF) of NiO-based p-i-n mixed-cation, mixed-halide perovskite solar cell was correlated with a light-induced strain relaxation.^[64] The relation between perovskite crystallinity and carrier dynamics has been further supported by different reports.^[65,66] For instance, lattice strain in perovskite films has been shown to correlate with the magnitude of nonradiative recombination.^[67] It is important to note that not enough has been known about the amorphous-crystalline perovskite interface, neither from a structural point of

view nor in terms of recombination pathways. In principle, an amorphous or nearly amorphous matrix is expected to have a large defect concentration, which should promote nonradiative recombination, detrimentally affecting the V_{OC} . Nonetheless, an enhancement of photoluminescence quantum yield in the vicinity of amorphous grain boundaries compared to grain interior was observed in a ≈ 30 μm -grain-sized MAPbBr₃ film.^[68] Similarly, Xing et al. demonstrated an efficient luminescence from amorphous perovskite nanoparticles.^[69] Notably, by simultaneously monitoring PV parameters and perovskite film formation, Alsari et al. observed a peak in the V_{OC} when a large amount of the perovskite precursor was not yet crystallized, pointing to a self-passivation effect by the amorphous starting material,^[70] which might apply to our case as well. Further discussion can be found in Note 2, Supporting Information.

Together with crystallinity, the morphology and chemical composition of the perovskite film are essential figures of merit in halide perovskite PV. To gain insights into the effect of biasing on perovskite film morphology and composition inside the device, a scanning transmission electron microscopy (STEM) characterization on cross sections of full devices was performed. **Figure 3a** shows the cross-sectional high-angle annular dark-field (HAADF) images of the fresh and biased samples. The comparison of the HAADF micrographs with and without biasing shows that the structural integrity of the device was preserved after bias. We did not detect any copper penetration from the electrode into the active layers underneath (Figure S9, Supporting Information). This indicated a negligible influence of the metal electrode on changes in the device J - V curves and optoelectronic properties.^[17] Further, Figure 3a shows changes in the spatial distribution of the relatively bright spots in the perovskite layer. These were distributed throughout the whole film in the fresh device but accumulated at both perovskite-selective contact interfaces after biasing. The higher

brightness of these spots relative to the bulk perovskite indicated their higher effective atomic number (Z_{eff}) as HAADF image intensity is roughly proportional to the square of Z_{eff} .

We treated the energy-dispersive X-ray (STEM-EDX) spectroscopic data with non-negative matrix factorization (NMF) for extraction of physically interpretable components to gain insight into the chemical composition of both the bulk perovskite and the bright spots (see Experimental Section or the study by Cacovich et al.^[71] for more details on this). Selected NMF components are displayed in Figure 3b,c and Figure S9, Supporting Information. The color of each pixel in a component's loading (map) indicated the relative contribution of that component's factor (spectrum) in that pixel's original EDX spectrum. Hence, Figure 3b shows the spatial distribution of iodine and lead while Figure 3c does the same for bromine and lead. The fresh perovskite device exhibited both iodine and bromine component as expected. However, we could see that after biasing, the iodine-rich phase became more dominant in the bulk of the perovskite layer (Figure 3b) while small bromine-rich areas formed at both perovskite-selective contact interfaces (Figure 3c).

Another exciting feature was the appearance of the red features (grains) in Figure 3b. These grains (representative grain is circled) were unique because they showed a substantial contribution (red pixels in Figure 3b) from the iodine-rich component but negligible contribution (dark blue pixels in Figure 3c) from the bromine-rich component. Since crystalline PbI₂ was revealed by XRD analysis, we proposed that these grains were PbI₂. Biasing reduced both the number and size of these grains (Figure 3b), in good agreement with our XRD data and suggested that there was a PbI₂ loss (e.g., a dissolution of these crystallites within the film). With similar reasoning, we could infer that the bromine-rich areas formed after biasing in Figure 3c were not representative of PbBr₂ because the NMF components showed a moderate iodine content in Figure 3b (area denoted by the rectangle). These grains' (areas') richness in lead and iodine (lead and bromine) agreed well with their high intensity in the HAADF images. We note that an amorphous window was reported in the compositional space of FAPb(I_xBr_{1-x})₃, when $0.3 < x < 0.5$.^[72] This could explain the lack of an evident shoulder at high angles for bromide-rich phase in XRD perovskite peaks (Figure 2c; Figure S4, Supporting Information) and GI-WAXS (Figure 2d; Figure S6, Supporting Information), despite the presence of those bromide-rich grains at the interfaces with selective contacts.

The above combination analysis from XRD, EL, and STEM indicated the occurrence of profound modifications to the perovskite layer upon biasing. We proposed that the charge trapping from iodide-rich domains, the morphologically degraded interfaces and the reduced charge transport and collection due to poor conductivity of the amorphized perovskite^[68,73] could explain the decrease of J_{SC} and FF driving the loss of the PCE. To support this hypothesis, we investigated the role of the iodide-rich phase by examining the modification in light absorption and photocurrent generation at wavelengths longer than 760 nm (band gap of the CsFAMA perovskite). **Figure 4a** shows the results of an in situ reflectance experiment on the biased devices near the band gap region (Figure S12, Supporting Information, shows the complete spectra in agreement with our previous work^[74]). Here, we observed a significant and

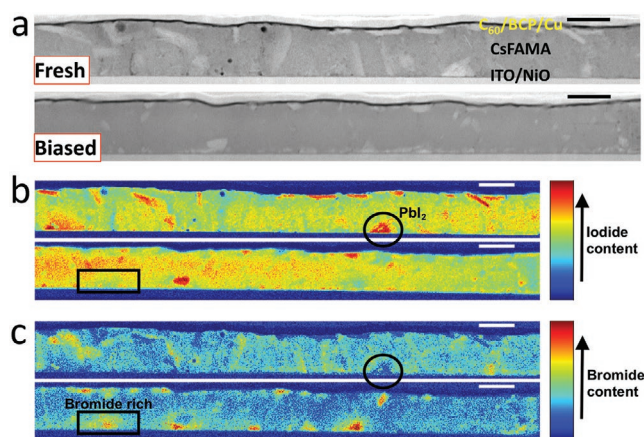


Figure 3. a) Cross-sectional STEM-HAADF micrographs for the fresh PSC (top) and after 12 h at 1.2 V bias in the dark (bottom). The dark circular spot in the STEM-HAADF micrograph for the fresh device arises from localized beam damage. b,c) NMF loadings (maps) of selected components, with the fresh sample at the top and biased sample at the bottom of each pair: b) iodide-rich perovskite phase and PbI₂ (see the main text for a detailed discussion) and c) bromide-rich perovskite phase. All scale bars are 0.5 μm . The micrographs and NMF maps for the fresh cell are reproduced with permission.^[121] Copyright 2019, Wiley-VCH.

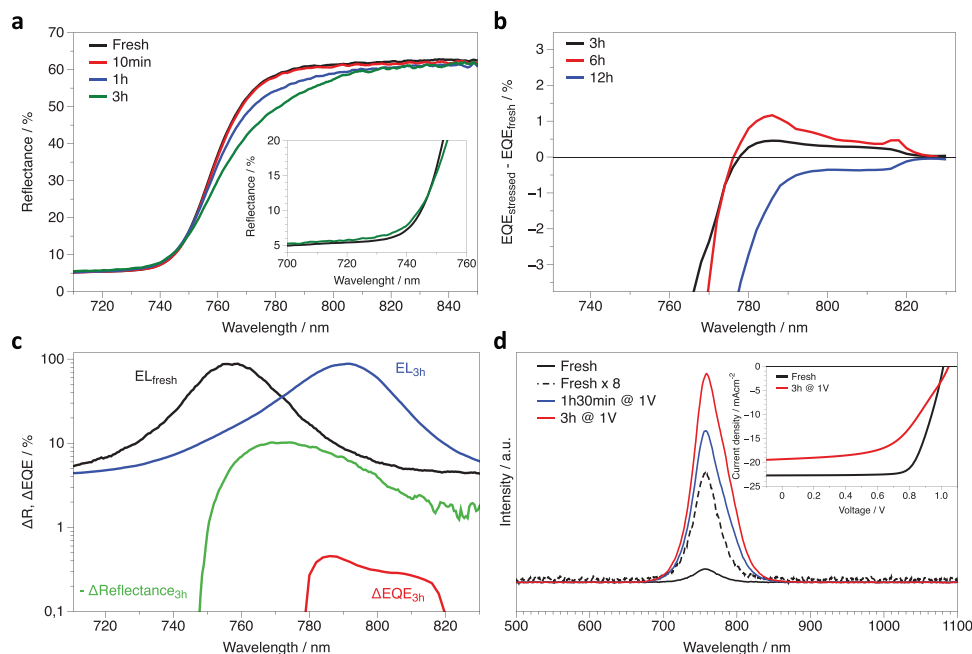


Figure 4. a) In situ reflectance experiment of full device biased at 1.2 V in the dark. The inset highlights the increase in reflectance attributable to the diminution of the original perovskite composition. b) Differential EQE ($\Delta EQE = EQE_{\text{biased}} - EQE_{\text{fresh}}$) around the band gap of the perovskite. The EQE is measured with a 2 nm step size. c) Comparison of variation in EQE (Figure 4b), reflectance (Figure 4a with the sign changed from negative to positive), and EL peak position (Figure 2e) after 3 h of biasing. The increase in the EQE at longer wavelengths is in close correlation with the light emission from the low band gap perovskite and the decrease of the reflectance. EL curves are plotted with respect to the x-axis (peak emission wavelength) only, for comparison with $-\Delta \text{Reflectance}_{3\text{h}}$ and $\Delta EQE_{3\text{h}}$. d) Evolution of EL peak upon biasing at 1.0 V (injected current density around 1 mA cm^{-2}). The inset highlights the effect of this stress test on $J-V$ curves.

gradual decrease of reflectance for wavelengths above 750 nm. This was accompanied by a small increase in the 720–745 nm range (see inset of Figure 4a, in agreement with the loss of the original perovskite composition due to amorphization). The decrease in reflectance above the band gap could stem from light absorption by the iodide rich phase as well as from an increase of energetic disorder of the perovskite, leading to a broader absorption onset (the two mechanisms could coexist). In Figure 4b, we show the differential external quantum efficiency (EQE) around the band gap of the perovskite, obtained by subtracting the EQE of the fresh device from the EQE after biasing ($EQE_{\text{biased}} - EQE_{\text{fresh}}$, see Experimental Section for more details on this analysis). Although the differential EQE was negative at wavelengths shorter than 750 nm (greater than 1.65 eV), remarkably, below the band gap ($>770 \text{ nm}$), EQE increased by 1–2% (absolute). This enhancement increased further with longer biasing (3–6 h), but then disappeared at 12 h. In Figure 4c, we compared the differential reflectance and EQE after 3 h of bias with the EL peak positions from the original CsFAMA and from the low band gap specimen. An excellent agreement was found between the small positive contribution to the EQE upon biasing ($\Delta EQE_{3\text{h}}$) and the EL peak governed by the iodide-rich phase, proving that the iodide-rich perovskite (inefficiently) contributes to the photocurrent.

For the sake of clarity, we stressed that the positive signal in the differential EQE above 770 nm was decidedly weak. Nonetheless, the conclusion that iodide-rich phase could contribute to the photo-current is supported by the analysis of PTAA-based devices (see Figure S13, Supporting Information),

for which the EQE below the band gap was markedly higher, implying that the efficiency of photocurrent generation from the low band gap domains depended also on the selective contacts. Notably, the selective contacts also influenced the device degradation pathways (discussion in conjunction with Figure S13, Supporting Information). To understand if charge trapping and inefficient photocurrent generation from iodide-rich domains were the primary sources of FF and J_{SC} losses, we performed a stress test at 1 V in the dark. In this case, the injected charge was markedly lower than at 1.2 V and appeared not enough to induce halide segregation^[37] as proven by the stable EL peak position (Figure 4d). Nonetheless, the effect on the $J-V$ curve was similar to what was obtained at 1.2 V, with a decrease in FF and J_{SC} and an increase of V_{OC} (see also Figure S3, Supporting Information). Interestingly, we found that the amorphization might occur regardless the halide segregation (see Figures S10 and S11, Supporting Information, together with the conjunction notes).

The evolution of the EQE upon biasing, as shown in Figure 5a, exhibited a substantial drop of EQE, especially at short wavelengths range (350–450 nm). The extinction coefficient of perovskite at short wavelengths is very high ($\approx 10^5 \text{ cm}^{-1}$),^[75] implying a steep hole-electron pair generation profile. Therefore, the EQE in this part of the spectrum is more sensitive to the quality of the interface closer to the direction of the incoming light (NiO/perovskite in this case). The high photocurrent loss in this short wavelength range, along with the worsened interfacial morphology observed in Figure 3, supported the hypothesis that perovskite amorphization was mainly

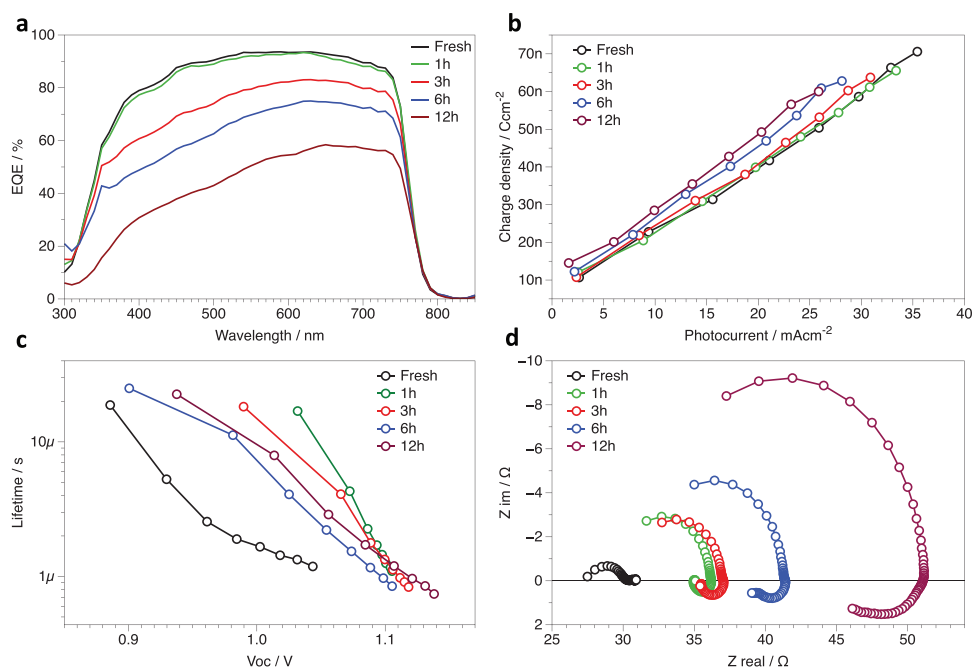


Figure 5. a) Variation in EQE upon biasing at 1.2 V in the dark showing asymmetry in the EQE reduction. b) Evolution of charge accumulation to the J_{SC} over biasing time as obtained from the CE experiment while biasing the device at 1.2 V in the dark. c) Evolution of carrier lifetimes to the V_{OC} over biasing time as obtained from the TPV experiment upon biasing the device at 1.2 V in the dark. d) Nyquist plot showing the evolution of the spectroscopic impedance at 1.2 V in the dark upon biasing the device in the same conditions.

localized at the interfaces. To gain more insights, we performed charge extraction (CE) experiments, which confirmed a lower J_{SC} for biased devices (Figure 5b; Figure S14, Supporting Information). The J_{SC} loss increased with the duration of the stress test and was more significant at high illumination levels. Interestingly, from the analysis of the charge density accumulated in the device and extracted only after the light pulse was switched off, it appeared that more recombination was introduced into the device upon biasing. In fact, at high illumination levels, we observed a decrease in both the photocurrent and the charge density extracted in dark, which implied that a more substantial part of the photo-generated charges recombined without being collected. This was in contrary with the higher V_{OC} and carrier lifetimes obtained from transient photovoltage (TPV) analysis after biasing (Figure 5c; Figure S15, Supporting Information). Hence, it was evidenced that the amorphous material introduced parasitic absorption, and thus reduced the number of photons reaching the crystalline and photoactive perovskite.

The reduction in interface quality was further confirmed by in situ electrochemical impedance spectroscopy (EIS) measurements, in which EIS was performed during biasing (Figure 5d). The spectrum for the fresh device was composed of two semicircles, as commonly observed for PSCs. Upon biasing, we observed a resistance increase in the high-frequency semicircle, which pointed to an increase in recombination resistance and charge transport/transfer resistance corroborating the above analysis.^[76,77] At the same time, the negative capacitance at low frequencies emerged. Several reports attributed the negative capacitance to the ion migration-induced modulation of the energetics at the perovskite/selective contact interfaces.^[78,79] For instance, Ebadi et al.^[79] observed a change from non-negative

capacitance devices to negative capacitance devices by doping Bi into the perovskite, due to the higher energy offset between TiO_2 - and the Bi-doped perovskite. In the dark condition, the negative capacitance was reported when there was a substantial barrier for the charge injection.^[78] In our case, the perovskite crystallinity loss was expected to impact the resistance associated with the charge injection, with the variation of the interface energetics also affected by a combination of the formation of ionic space charge and changes in the halide composition and morphology at the interface. Overall, this finding further confirmed the bias-driven interfacial degradation in mixed halide PSCs.

3. Conclusion

In this study, we investigated the reasons underlying PCE losses of PSCs due to ion migration. Our results show that bias-driven ion migration in planar PSCs induces the amorphization of perovskite and halide segregation when enough charge is injected into the device. The V_{OC} increase might be likely explained by taking into account the perovskite self-doping effect due to the formation of ionic space charge at the interfaces. However, the halide segregation and the loss in perovskite crystallinity contribute to hinder the charge collection, significantly reducing J_{SC} and FF, and thus PCE. The ion migration-driven amorphization of perovskite might be a fundamental degradation mechanism for optoelectronic devices. As a solution strategy, we believe that fine compositional engineering^[80] or the introduction of additives into the perovskite^[40,81] might be suitable. In the preliminary tests presented, it appears that the bias-induced degradation is

dominant even when light shines on the device or at high temperature. Nonetheless, the overlapping effects of bias-induced perovskite amorphization, thermal decomposition, and light-induced degradation are critical topics for further investigation, to disentangle each specific mechanism. As a final consideration, the ion migration-induced loss of perovskite crystallinity might have consequences for characterization techniques based on prolonged DC polarization, employed, for example, to investigate ion migration in lead halide perovskites, and therefore should be taken into account.

4. Experimental Section

Electron Selective Layer Deposition: For substrate cleaning, patterned indium tin oxide (ITO) glass substrates (25 mm × 25 mm, 15 Ωsq⁻¹, patterned by Automatic Research GmbH), cleaned for 20 min with Mucosal 2% solution in deionized water, acetone, and isopropanol in an ultrasonic bath, were treated in an UV-ozone cleaner for 15 min.

The nickel oxide layer was deposited from a 0.15 M NiCl₂·6H₂O (Alfa Aesar) solution in anhydrous 2-methoxyethanol (99.8%, Sigma-Aldrich) with the addition of 20 μL mL⁻¹ HNO₃ 65% (Sigma-Aldrich). After shaking the solution overnight at 60 °C, the spin-coating deposition of NiO was via the following program: 500 rpm (1 s acceleration) for 1 s and 4000 rpm (2 s acceleration) for 30 s. After the spin-coating, the substrate was dried sequentially at 75 °C for 10 min, at 120 °C for 15 min and then annealed at 300 °C for 1 h.

For PTAA layer, PTAA (Sigma-Aldrich) was dissolved at a concentration of 2 mg mL⁻¹ in anhydrous toluene (Sigma-Aldrich). The deposition was performed by spin-coating at 5000 rpm for 30 s and annealing at 100 °C for 10 min in glove box.

Perovskite Layer Deposition: For Cs_{0.05}((FAPbI₃)_{0.83}(MAPbBr₃)_{0.17})_{0.95} perovskite, PbBr₂ (1.5 M) and PbI₂ (1.5 M) were dissolved in a mixture of anhydrous DMF/DMSO (4:1 volume ratio) (Sigma-Aldrich) and added to FAI (1.09:1 molar ratio) and MABr (1.09:1 molar ratio) powders respectively, to obtain MAPbBr₃ and FAPbI₃ solutions with a final concentration of 1.24 M. These two solutions were then mixed in a 17:83 volume ratio. Finally, the cesium cation was added from a 1.5 M CsI solution in DMSO in a 5:95 volume ratio. The perovskite solution was spin-coated on top of the hole selective layer using the following program: 4000 rpm (5 s acceleration) for 35 s (total time: 40 s). After 25 s, 500 μL ethyl acetate was dropped on the spinning substrate. After the spin-coating program, the perovskite-coated sample was annealed at 100 °C for 60 min on a hotplate. For the Cs_{0.05}((FAPbI₃)_{0.83}(MAPbBr₃)_{0.17})_{0.95} perovskite, the same procedure as for the Cs_{0.05}((FAPbI₃)_{0.83}(MAPbBr₃)_{0.17})_{0.95} composition was followed, just modifying the solution composition to obtain the desired stoichiometry. The MAPbI₃ perovskite precursor was 1.2 M of PbI₂ (Tokyo Chemical Industry), and CH₃NH₃I (Dyename) in mixed solvent of DMF/DMSO (6:1 volume ratio). The solution was put in thermal shaker at 60 °C for 5 min. The spin-coating program for MAPbI₃ was with 4000 rpm for 30 s, ramping for 5 s. A total of 500 μL of ethyl acetate was used as antisolvent quenching step after 20 s of spin-coating.

Electron Selective Layers and Metal Electrode Deposition: On top of the perovskite, 23 nm C₆₀ and 8 nm BCP were deposited by thermal evaporation (MBRAUN PROvap 3G) with evaporation rates below 0.2 Å s⁻¹ at a pressure of under 1E-6 mbar. Finally, 100 nm Cu was evaporated at a rate of 0.08–1.0 Å s⁻¹. The active area was defined by the overlap of patterned ITO and the metal electrode, which was 0.16 cm².

PV Performances Characterization: *J*-*V* characteristics under 1 sun equivalent illumination were recorded using a WAVELABS SINUS-70 LED class AAA calibrated with a silicon reference solar cell from Fraunhofer ISE. *J*-*V* scans were performed with a Keithley 2400 SMU, controlled by a measurement control program written in LabVIEW. The voltage values were swept in 20 mV steps with variable integration time and settling time after voltage application to control the scan rate.

Optoelectronics Characterization: TPV, CE, IPCE, and EL were performed with a commercial modular instrument for advanced photoelectrical characterization (Arkeo from Cicci Research s.r.l.). In the case of TPV and CE, the setup was based on a high-speed waveform generator that drives a high-speed LED (5000 K). The device was connected to a transimpedance amplifier and a differential voltage amplifier to monitor short circuit current or open circuit voltage. The light intensity could be varied between 0.1 and 2 equivalent suns. EQE analysis was performed with a commercial apparatus (Arkeo) based on a 300 W xenon lamp monochromatic light (300–1100 nm at 2 nm of resolution) with thermal-controlled stage. A source meter with 1 pA of resolution was directly connected to the device and NIST-calibrated silicon detector. For the differential EQE shown in Figure 5b,c, the EQE between 700 and 830 nm was recorded with 2 nm of resolution. EL spectra were recorded with a commercial apparatus (Arkeo) composed by a CCD spectrometer. The devices were biased employing the same setup. The EL spectra were acquired at a driving voltage of 2.25 V and with a fast acquisition time (the measurement takes less than 5 s). The fast acquisition time assured that the halide segregation was not induced by the high current density (above 100 mA cm⁻²) during the acquisition time, as shown in Figure 5d. The optical coupling system was composed of a lens condenser attached to a multimode optical fiber bundle. The Arkeo apparatus allowed overlapping a constant biasing to TPV, CE, EQE, EL, and other techniques. The bias was applied continuously and switched off only during the measurements described. Impedance spectroscopy was performed with an FRA-equipped SolarLab XM potentiostat.

In Situ X-Ray Diffraction and GI-XRD: The biasing was performed with a high-precision source meter directly connected within the XRD chamber. The samples had to be shipped to perform this experiment, and this is probably the reason behind the relatively higher content of PbI₂ found in the diffractograms, with respect to what was found when characterizing the cells where fabricated (see, for instance, the study by De Wolf et al.^[74]). XRD was performed using a PANalytical X'Pert Pro MPD diffractometer (Cu Kα radiation), with patterns collected continuously (the time required to collect a single diffractogram is 1 h). More details on the experiment are provided in Figure S4, Supporting Information. It must be noted that the diameter of the incident X-ray beam was 1 cm at the sample surface, while the width of one cell was 0.4 cm. For the measurement done with 1 V as shown in Figure S10, Supporting Information, grazing-incidence geometry with a smaller slit was used, and hence, the beam spot had diameter of 0.45 cm that was also bigger than the cell's area. Therefore, XRD patterns were collected partially from the adjacent unbiased area, thus quantitative analysis underestimated the observed phenomena. A duplicate XRD measurement without biasing was done to exclude the possibility of X-ray beam-induced perovskite damage influencing the results. In this control experiment, no changes were observed in the diffraction patterns after 8 hourly scans (Figure S3, Supporting Information).

In Situ Reflectance: In situ reflectance spectra were acquired with a UV–vis 2550 spectrophotometer from Shimadzu, calibrated with BaSO₄. The biasing was performed during the measurement with a Keithley 2400 SMU with analogue control.

STEM Characterization: Cross-sectional lamellae of fresh and biased (12 h at 1.2 V in dark) devices were prepared and thinned to electron transparency by focused ion beam milling (FEI Helios NanoLab DualBeam FIB/SEM) using a standard protocol^[82] with minimal (≈2 min) exposure to air between lamella preparation and STEM characterization. For the biased device, lamella milling was performed immediately after the biasing regime was completed. Cross-sectional HAADF imaging and EDX spectroscopy were carried out in a FEI Tecnai Osiris operated at 200 kV and equipped with a Bruker Super-X EDX silicon drift detector with a total collection solid angle of ≈0.9 sr. To minimize beam damage, EDX spectrum images were acquired with a defocused beam (Δ*f* = -0.5 μm), probe current of ≈250 pA, spatial sampling of 10 nm per pixel, and dwell time of 50 ms per pixel. Data were acquired with Tecnai Imaging and Analysis and analyzed with

HyperSpy.^[83] The data were treated with NMF for decomposition into easily identifiable components.

In Situ Grazing-Incidence Synchrotron Wide-Angle X-Ray Scattering: Grazing-incidence synchrotron wide-angle X-ray scattering data were acquired at the KMC2 beamline at BESSY II synchrotron (Helmholtz Zentrum Berlin). Samples were biased in situ in air and in the dark and scattered X-rays were acquired at a range of scattering angles every 15 min, at grazing incidence angles of 2° and 4°, through the Cu top contact. The photon energy of the beam was set to 8048 eV, matching Cu K α radiation.

MD Simulation: The simulated defect-free and defected samples were aged at constant pressure and temperature at ambient conditions for a total of \approx 500 ps. The samples were obtained starting from a system containing 256 MAPI₃ stoichiometric units in which defects were introduced randomly. Simulations were performed using the MYP1 force model^[84,85] using the LAMMPS code.^[86]

Supporting Information

Supporting Information is available from the Wiley Online Library or from the author.

Acknowledgements

D.D.G. and N.P. contributed equally to this work. The authors thank Helmholtz Zentrum Berlin (HZB) for the beamtime at together with Dr. Daniel Többens, Dr. Rahim Munir, and Hampus Näsström for their kind assistance during the beamtime. D.D.G. thanks the Ph.D. program of the University of Rome, La Sapienza. N.P. thanks the Ph.D. program of University of Potsdam. D.D.G. and N.P. thank Amran Al-Ashouri for the support in device fabrication. F.U.K. thanks the Jardine Foundation and Cambridge Trust for a doctoral scholarship. F.U.K., G.D., and C.D. thank Tiarnan A. S. Doherty and Dr. Samuel D. Stranks (Cavendish Laboratory, University of Cambridge) for assistance in biasing devices for TEM characterization. The research leading to these results received funding from the European Union Horizon 2020 research and innovation program under grant agreement number 823717—ESTEEM3. D.D. and A.L. acknowledge the financial support from MIUR (Project PRIN 2017 with title Novel Multilayered and Micro-Machined Electrode Nano-Architectures for Electrocatalytic Applications—Prot. 2017YH9MRK). D.D. also acknowledges the financial support from the University of Rome, La Sapienza (Project ATENEO 2019 Prot. RM11916B756961CA). F.D.G. thanks ESPResSo project (Horizon 2020, grant 764047). S.H.T.C. thanks CONACYT-México for support. L.C. thanks ARIADNE project (POR-FESR 2014–2020). A.D.C. gratefully acknowledge the financial support from the Ministry of Education and Science of the Russian Federation in the framework of MegaGrant (no. 075-15-2019-872 (14.Y26.31.0027/074-02-2018-327)). J.A.S. thanks EPSRC and Prof. David Lidzey for Ph.D. studentship funding via CDT-PV (EP/L01551X/1).

Conflict of Interest

The authors declare no conflict of interest.

Keywords

amorphization, degradation mechanism, halide perovskites, ion migration, perovskite solar cells, phase segregation, potential-induced degradation

Received: January 23, 2020

Revised: March 27, 2020

Published online:

- [1] NREL Best Research-Cell Efficiencies, <https://www.nrel.gov/pv/assets/pdfs/pv-efficiencies> (accessed: January 2020).
- [2] A. Kojima, K. Teshima, Y. Shirai, T. Miyasaka, *J. Am. Chem. Soc.* **2009**, *131*, 6050.
- [3] S. D. Stranks, G. E. Eperon, G. Grancini, C. Menelaou, M. J. P. Alcocer, T. Leijtens, L. M. Herz, A. Petrozza, H. J. Snaith, *Science* **2013**, *342*, 341.
- [4] S. de Wolf, J. Holovsky, S.-J. Moon, P. Löper, B. Niesen, M. Ledinsky, F. Haug, J. Yum, C. Ballif, *J. Phys. Chem. C* **2014**, *5*, 1035.
- [5] G. E. Eperon, S. D. Stranks, C. Menelaou, M. B. Johnston, L. M. Herz, H. J. Snaith, *Energy Environ. Sci.* **2014**, *7*, 982.
- [6] R. J. Sutton, G. E. Eperon, L. Miranda, E. S. Parrott, B. A. Kamino, J. B. Patel, M. T. Hörantner, M. B. Johnston, A. A. Haghghirad, D. T. Moore, H. J. Snaith, *Adv. Energy Mater.* **2016**, *6*, 1502458.
- [7] E. L. Unger, L. Kegelmann, K. Suchan, D. Sörell, L. Korte, S. Albrecht, *J. Mater. Chem. A* **2017**, *5*, 11401.
- [8] K. A. Bush, A. F. Palmstrom, Z. J. Yu, M. Boccard, R. Cheacharoen, J. P. Mailoa, D. P. McMeekin, R. L. Z. Hoye, C. D. Bailie, T. Leijtens, I. M. Peters, M. C. Minichetti, N. Rolston, R. Prasanna, S. Sofia, D. Harwood, W. Ma, F. Moghadam, H. J. Snaith, T. Buonassisi, Z. C. Holman, S. F. Bent, M. D. McGehee, *Nat. Energy* **2017**, *2*, 17009.
- [9] C. Yi, J. Luo, S. Meloni, A. Boziki, N. Ashari-Astani, C. Grätzel, S. M. Zakeeruddin, U. Röhrlisberger, M. Grätzel, *Energy Environ. Sci.* **2016**, *9*, 656.
- [10] D. P. McMeekin, G. Sadoughi, W. Rehman, G. E. Eperon, M. Saliba, M. T. Hörantner, A. Haghghirad, N. Sakai, L. Korte, B. Rech, M. B. Johnston, L. M. Herz, H. J. Snaith, *Science* **2016**, *351*, 151.
- [11] A. Binek, F. C. Hanusch, P. Docampo, T. Bein, *J. Phys. Chem. Lett.* **2015**, *6*, 1249.
- [12] M. Saliba, T. Matsui, J. Y. Seo, K. Domanski, J. P. Correa-Baena, M. K. Nazeeruddin, S. M. Zakeeruddin, W. Tress, A. Abate, A. Hagfeldt, M. Grätzel, *Energy Environ. Sci.* **2016**, *9*, 1989.
- [13] G. Richardson, S. E. J. O'Kane, R. G. Niemann, T. A. Peltola, J. M. Foster, P. J. Cameron, A. B. Walker, *Energy Environ. Sci.* **2016**, *9*, 1476.
- [14] H. J. Snaith, A. Abate, J. M. Ball, G. E. Eperon, T. Leijtens, N. K. Noel, S. D. Stranks, J. T.-W. Wang, K. Wojciechowski, W. Zhang, *J. Phys. Chem. Lett.* **2014**, *5*, 1511.
- [15] K. Domanski, B. Roose, T. Matsui, M. Saliba, S. H. Turren-Cruz, J. P. Correa-Baena, C. R. Carmona, G. Richardson, J. M. Foster, F. De Angelis, J. M. Ball, A. Petrozza, N. Mine, M. K. Nazeeruddin, W. Tress, M. Grätzel, U. Steiner, A. Hagfeldt, A. Abate, *Energy Environ. Sci.* **2017**, *10*, 604.
- [16] G. Kakavelakis, I. Paradisanos, B. Paci, A. Generosi, M. Papachatzakis, T. Maksudov, L. Najafi, A. E. Del Rio Castillo, G. Kioseoglou, E. Stratakis, F. Bonaccorso, E. Kymakis, *Adv. Energy Mater.* **2018**, *8*, 1702287.
- [17] A. Guerrero, J. You, C. Aranda, Y. S. Kang, G. Garcia-Belmonte, H. Zhou, J. Bisquert, Y. Yang, *ACS Nano* **2016**, *10*, 218.
- [18] K. Domanski, J. P. Correa-Baena, N. Mine, M. K. Nazeeruddin, A. Abate, M. Saliba, W. Tress, A. Hagfeldt, M. Grätzel, *ACS Nano* **2016**, *10*, 6306.
- [19] S. Cacovich, L. Ciná, F. Matteocci, G. Divitini, P. A. Midgley, A. Di Carlo, C. Ducati, *Nanoscale* **2017**, *9*, 4700.
- [20] L. A. Frolova, N. N. Dremova, P. A. Troshin, *Chem. Commun.* **2015**, *51*, 14917.
- [21] D. Di Girolamo, F. Matteocci, F. U. Kosasih, G. Chistiakova, W. Zuo, G. Divitini, L. Korte, C. Ducati, A. Di Carlo, D. Dini, A. Abate, *Adv. Energy Mater.* **2019**, *9*, 1901642.
- [22] J. Carrillo, A. Guerrero, S. Rahimnejad, O. Almora, I. Zarazua, E. Mas-Marza, J. Bisquert, G. Garcia-Belmonte, *Adv. Energy Mater.* **2016**, *6*, 1502246.
- [23] T. Sekimoto, T. Matsui, T. Nishihara, R. Uchida, T. Sekiguchi, T. Negami, *ACS Appl. Energy Mater.* **2019**, *2*, 5039.

- [24] R. A. Kerner, B. P. Rand, *ACS Appl. Energy Mater.* **2019**, *2*, 6097.
- [25] J. Pospisil, A. Guerrero, O. Zmeskal, M. Weiter, J. J. Gallardo, J. Navas, G. Garcia-Belmonte, *Adv. Funct. Mater.* **2019**, *29*, 1900881.
- [26] S. Wu, R. Chen, S. Zhang, B. H. Babu, Y. Yue, H. Zhu, Z. Yang, C. Chen, W. Chen, Y. Huang, S. Fang, T. Liu, L. Han, W. Chen, *Nat. Commun.* **2019**, *10*, 1161.
- [27] H. J. Jung, D. Kim, S. Kim, J. Park, V. P. Dravid, B. Shin, *Adv. Mater.* **2018**, *30*, 1802769.
- [28] Q. Jeangros, M. Duchamp, J. Werner, M. Kruth, R. E. Dunin-Borkowski, B. Niesen, C. Ballif, A. Hessler-Wyser, *Nano Lett.* **2016**, *16*, 7013.
- [29] C. Li, A. Guerrero, Y. Zhong, A. Gräser, C. A. M. Luna, J. Köhler, J. Bisquert, R. Hildner, S. Huettner, *Small* **2017**, *13*, 1701711.
- [30] T. Leijtens, E. T. Hoke, G. Grancini, D. J. Slotcavage, G. E. Eperon, J. M. Ball, M. De Bastiani, A. R. Bowring, N. Martino, K. Wojciechowski, M. D. McGehee, H. J. Snaith, A. Petrozza, *Adv. Energy Mater.* **2015**, *5*, 1500962.
- [31] X. Deng, X. Wen, C. F. J. Lau, T. Young, J. Yun, M. A. Green, S. Huang, A. W. Y. Ho-Baillie, *J. Mater. Chem. C* **2016**, *4*, 9060.
- [32] A. Rizzo, F. Lamberti, M. Buonomo, N. Wrachien, L. Torto, N. Lago, S. Sansoni, R. Pilot, M. Prato, N. Michieli, M. Meneghetti, G. Meneghesso, A. Cester, *Sol. Energy Mater. Sol. Cells* **2019**, *189*, 43.
- [33] B. Chen, T. Li, Q. Dong, E. Mosconi, J. Song, Z. Chen, Y. Deng, Y. Liu, S. Ducharme, A. Gruverman, F. De Angelis, J. Huang, *Nat. Mater.* **2018**, *17*, 1020.
- [34] D. Kim, J. S. Yun, P. Sharma, D. S. Lee, J. Kim, A. M. Soufiani, S. Huang, M. A. Green, A. W. Y. Ho-Baillie, J. Seidel, *Nat. Commun.* **2019**, *10*, 444.
- [35] S. Y. Luchkin, A. F. Akbulatov, L. A. Frolova, M. P. Griffin, A. Dolocan, R. Gearba, D. A. V. Bout, P. A. Troshin, K. J. Stevenson, *ACS Appl. Mater. Interfaces* **2017**, *9*, 33478.
- [36] C. G. Bischak, C. L. Hetherington, H. Wu, S. Aloni, D. F. Ogletree, D. T. Limmer, N. S. Ginsberg, *Nano Lett.* **2017**, *17*, 1028.
- [37] I. L. Braly, R. J. Stoddard, A. Rajagopal, A. R. Uhl, J. K. Katahara, A. K. Jen, H. W. Hillhouse, *ACS Energy Lett.* **2017**, *2*, 1841.
- [38] G. F. Samu, Á. Balog, F. De Angelis, D. Meggiolaro, P. V. Kamat, C. Janáky, *J. Am. Chem. Soc.* **2019**, *141*, 10812.
- [39] M. Najafi, F. Di Giacomo, D. Zhang, S. Shanmugam, A. Senes, W. Verhees, A. Hadipour, Y. Galagan, T. Aernouts, S. Veenstra, R. Andriessen, *Small* **2018**, *14*, 1702775.
- [40] S. Bai, P. Da, C. Li, Z. Wang, Z. Yuan, F. Fu, M. Kawecky, X. Liu, N. Sakai, J. T. Wang, S. Huettner, S. Buecheler, M. Fahlman, F. Gao, H. J. Snaith, *Nature* **2019**, *571*, 245.
- [41] W. Chen, Y. Zhou, L. Wang, Y. Wu, B. Tu, B. Yu, F. Liu, H.-W. Tam, G. Wang, A. B. Djurišić, L. Huang, Z. He, *Adv. Mater.* **2018**, *30*, 1800515.
- [42] T. Abzieher, S. Moghadamzadeh, F. Schackmar, H. Eggers, F. Sutterlüti, A. Farooq, D. Kojda, K. Habicht, R. Schmager, A. Mertens, R. Azmi, L. Klotz, J. A. Schwenzler, M. Hetterich, U. Lemmer, B. S. Richards, M. Powalla, U. W. Paetzold, *Adv. Energy Mater.* **2019**, *9*, 1802995.
- [43] I. J. Park, G. Kang, M. A. Park, J. S. Kim, S. W. Seo, D. H. Kim, K. Zhu, T. Park, J. Y. Kim, *ChemSusChem* **2017**, *10*, 2660.
- [44] C. Hu, Y. Bai, S. Xiao, T. Zhang, X. Meng, W. K. Ng, Y. Yang, K. S. Wong, H. Chen, S. Yang, *J. Mater. Chem. A* **2017**, *5*, 21858.
- [45] M. V. Khenkin, E. A. Katz, A. Abate, G. Bardizza, J. J. Berry, C. Brabec, F. Brunetti, V. Bulović, Q. Burlingame, A. Di Carlo, R. Cheacharoen, Y.-B. Cheng, A. Colmann, S. Cros, K. Domanski, M. Dusza, C. J. Fell, S. R. Forrest, Y. Galagan, D. Di Girolamo, M. Grätzel, A. Hagfeldt, E. von Hauff, H. Hoppe, J. Kettle, H. Köbler, M. S. Leite, S. Liu, Y.-L. Loo, J. M. Luther, C.-Q. Ma, M. Madsen, M. Manca, M. Matheron, M. McGehee, R. Meitzner, M. K. Nazeeruddin, A. F. Nogueira, C. Odabaşı, A. Osherov, N.-G. Park, M. O. Reese, F. De Rossi, M. Saliba, U. S. Schubert, H. J. Snaith, S. D. Stranks, W. Tress, P. A. Troshin, V. Turkovic, S. Veenstra, I. Visoly-Fisher, A. Walsh, T. Watson, H. Xie, R. Yildirim, S. M. Zakeeruddin, K. Zhu, M. Lira-Cantu, *Nat. Energy* **2020**, *5*, 35.
- [46] F. Wu, B. Bahrami, K. Chen, S. Mabrouk, R. Pathak, Y. Tong, X. Li, T. Zhang, R. Jian, Q. Qiao, *ACS Appl. Mater. Interfaces* **2018**, *10*, 25604.
- [47] Y. Deng, Z. Xiao, J. Huang, *Adv. Energy Mater.* **2015**, *5*, 1500721.
- [48] Z. Xiao, Y. Yuan, Y. Shao, Q. Wang, Q. Dong, C. Bi, P. Sharma, A. Gruverman, J. Huang, *Nat. Mater.* **2015**, *14*, 193.
- [49] L.-Q. Xie, L. Chen, Z.-A. Nan, H.-X. Lin, T. Wang, D.-P. Zhan, J.-W. Yan, B.-W. Mao, Z.-Q. Tian, *J. Am. Chem. Soc.* **2017**, *139*, 3320.
- [50] C. Giacomazzo, H. L. Monaco, G. Artioli, D. Viterbo, M. Milanesio, G. Gilli, P. Gilli, G. Zanotti, G. Ferraris, M. Catti, *Fundamentals of Crystallography*, Oxford University Press, Oxford **2011**.
- [51] D. Di Girolamo, M. I. Dar, D. Dini, L. Gontrani, R. Caminiti, A. Mattoni, M. Graetzel, S. Meloni, *J. Mater. Chem. A* **2019**, *7*, 12292.
- [52] Y. Yuan, Q. Wang, Y. Shao, H. Lu, T. Li, A. Gruverman, J. Huang, *Adv. Energy Mater.* **2016**, *6*, 1501803.
- [53] P. Lopez-Varo, J. A. Jiménez-Tejada, M. García-Rosell, J. A. Anta, S. Ravishankar, A. Bou, J. Bisquert, *ACS Energy Lett.* **2017**, *2*, 1450.
- [54] C. Caddeo, A. Filippetti, A. Mattoni, *Nano Energy* **2020**, *67*, 104162.
- [55] M. A. Krivoglaz, *X-Ray and Neutron Diffraction in Nonideal Crystals*, Springer, Berlin **2012**.
- [56] Z. Andaji-Garmaroudi, M. Abdi-Jalebi, D. Guo, S. Macpherson, A. Sadhanala, E. M. Tennyson, E. Ruggeri, M. Anaya, K. Galkowski, R. Shivanna, K. Lohmann, K. Frohna, S. Mackowski, T. J. Savenije, R. H. Friend, S. D. Stranks, *Adv. Mater.* **2019**, *31*, 1902374.
- [57] E. T. Hoke, D. J. Slotcavage, E. R. Dohner, A. R. Bowring, H. I. Karunadasa, M. D. McGehee, *Chem. Sci.* **2015**, *6*, 613.
- [58] F. Ruf, P. Rietz, M. F. Aygüler, I. Kelz, P. Docampo, H. Kalt, M. Hetterich, *ACS Energy Lett.* **2018**, *3*, 2995.
- [59] L. T. Schelhas, Z. Li, J. A. Christians, A. Goyal, P. Kairys, S. P. Harvey, D. H. Kim, K. H. Stone, J. M. Luther, K. Zhu, V. Stevanovic, J. J. Berry, *Energy Environ. Sci.* **2019**, *12*, 1341.
- [60] S. G. Motti, D. Meggiolaro, A. J. Barker, E. Mosconi, C. A. R. Perini, J. M. Ball, M. Gandini, M. Kim, F. De Angelis, A. Petrozza, *Nat. Photonics* **2019**, *13*, 532.
- [61] D. W. DeQuilettes, W. Zhang, V. M. Burlakov, D. J. Graham, T. Leijtens, A. Osherov, V. Bulović, H. J. Snaith, D. S. Ginger, S. D. Stranks, *Nat. Commun.* **2016**, *7*, 11683.
- [62] A. Merdasa, M. Bag, Y. Tian, E. Källman, A. Dobrovolsky, I. G. Scheblykin, *J. Phys. Chem. C* **2016**, *120*, 10711.
- [63] L. Zhao, J. Gao, Y. L. Lin, Y. Yeh, K. M. Lee, N. Yao, Y. Loo, B. P. Rand, *Adv. Mater.* **2017**, *29*, 1605317.
- [64] H. Tsai, R. Asadpour, J. C. Blancon, C. C. Stoumpos, O. Durand, J. W. Strzalka, B. Chen, R. Verduzco, P. M. Ajayan, S. Tretiak, J. Even, M. A. Alam, M. G. Kanatzidis, W. Nie, A. D. Mohite, *Science* **2018**, *360*, 67.
- [65] C. Zhu, X. Niu, Y. Fu, N. Li, C. Hu, Y. Chen, X. He, G. Na, P. Liu, H. Zai, Y. Ge, Y. Lu, X. Ke, Y. Bai, S. Yang, P. Chen, Y. Li, M. Sui, L. Zhang, H. Zhou, Q. Chen, *Nat. Commun.* **2019**, *10*, 815.
- [66] L. Zhang, W. Geng, C. Tong, X. Chen, T. Cao, M. Chen, *Sci. Rep.* **2018**, *8*, 7760.
- [67] T. W. Jones, A. Osherov, M. Alsari, M. Sponseller, B. C. Duck, Y.-K. Jung, C. Settens, F. Niroui, R. Brenes, C. V. Stan, Y. Li, M. Abdi-Jalebi, N. Tamura, J. E. Macdonald, M. Burghammer, R. H. Friend, V. Bulović, A. Walsh, G. J. Wilson, S. Lilliu, S. D. Stranks, *Energy Environ. Sci.* **2019**, *12*, 596.
- [68] G. W. P. Adhyaksa, S. Brittman, H. Āboliņš, A. Lof, X. Li, J. D. Keelor, Y. Luo, T. Duevski, R. M. A. Heeren, S. R. Ellis, D. P. Fenning, E. C. Garnett, *Adv. Mater.* **2018**, *30*, 1804792.
- [69] J. Xing, F. Yan, Y. Zhao, S. Chen, H. Yu, Q. Zhang, R. Zeng, H. V. Demir, X. Sun, A. Huan, Q. Xiong, *ACS Nano* **2016**, *10*, 6623.
- [70] M. Alsari, O. Bikondoa, J. Bishop, M. Abdi-Jalebi, L. Y. Ozer, M. Hampton, P. Thompson, M. T. Hörantner, S. Mahesh, C. Greenland, J. E. Macdonald, G. Palmisano, H. J. Snaith, D. G. Lidzey, S. D. Stranks, R. H. Friend, S. Lilliu, *Energy Environ. Sci.* **2018**, *11*, 383.

- [71] S. Cacovich, F. Matteocci, M. Abdi-Jalebi, S. D. Stranks, A. Di Carlo, C. Ducati, G. Divitini, *ACS Appl. Energy Mater.* **2018**, *1*, 7174.
- [72] W. Rehman, R. L. Milot, G. E. Eperon, C. Wehrenfennig, J. L. Boland, H. J. Snaith, M. B. Johnston, L. M. Herz, *Adv. Mater.* **2015**, *27*, 7938.
- [73] Y. Wang, X. Lü, W. Yang, T. Wen, L. Yang, X. Ren, L. Wang, Z. Lin, Y. Zhao, *J. Am. Chem. Soc.* **2015**, *137*, 11144.
- [74] D. Di Girolamo, N. Phung, M. Jošt, A. Al-Ashouri, G. Chistiakova, J. Li, J. A. Márquez, T. Unold, L. Korte, S. Albrecht, A. Di Carlo, D. Dini, A. Abate, *Adv. Mater. Interfaces* **2019**, *6*, 1900789.
- [75] S. De Wolf, J. Holovsky, S. J. Moon, P. Löper, B. Niesen, M. Ledinsky, F. J. Haug, J. H. Yum, C. Ballif, *J. Phys. Chem. Lett.* **2014**, *5*, 1035.
- [76] A. Guerrero, G. Garcia-Belmonte, I. Mora-Sero, J. Bisquert, Y. S. Kang, T. J. Jacobsson, J. P. Correa-Baena, A. Hagfeldt, *J. Phys. Chem. C* **2016**, *120*, 8023.
- [77] A. Pockett, G. E. Eperon, N. Sakai, H. J. Snaith, L. M. Peter, P. J. Cameron, *Phys. Chem. Chem. Phys.* **2017**, *19*, 5959.
- [78] D. Moia, I. Gelmetti, P. Calado, W. Fisher, M. Stringer, O. Game, Y. Hu, P. Docampo, D. Lidzey, E. Palomares, J. Nelson, P. R. F. Barnes, *Energy Environ. Sci.* **2019**, *12*, 1296.
- [79] F. Ebadi, N. Taghavinia, R. Mohammadpour, A. Hagfeldt, W. Tress, *Nat. Commun.* **2019**, *10*, 1574.
- [80] T. Matsui, T. Yamamoto, T. Nishihara, R. Morisawa, T. Yokoyama, T. Sekiguchi, T. Negami, *Adv. Mater.* **2019**, *31*, 1806823.
- [81] N. Li, S. Tao, Y. Chen, X. Niu, C. K. Onwudinanti, C. Hu, Z. Qiu, Z. Xu, G. Zheng, L. Wang, Y. Zhang, L. Li, H. Liu, Y. Lun, J. Hong, X. Wang, Y. Liu, H. Xie, Y. Gao, Y. Bai, S. Yang, G. Brocks, Q. Chen, H. Zhou, *Nat. Energy* **2019**, *4*, 408.
- [82] F. U. Kosasih, C. Ducati, *Nano Energy* **2018**, *47*, 243.
- [83] F. de la Pena, T. Ostasevicius, V. T. Fauske, P. Burdet, P. Jokubauskas, M. Sarahan, D. Johnstone, M. Nord, J. Taillon, J. Caron, K. E. MacArthur, E. Prestat, A. Eljarrat, S. Mazzucco, T. Furnival, M. Walls, G. Donval, B. Martineau, A. Garmannslund, L. F. Zagonel, T. Aarholt, C. Gohlke, I. Iyengar, *Microsc. Microanal.* **2017**, *23*, 214.
- [84] A. Mattoni, A. Filippetti, M. I. Saba, P. Delugas, *J. Phys. Chem. C* **2015**, *119*, 17421.
- [85] C. Caddeo, M. I. Saba, S. Meloni, A. Filippetti, A. Mattoni, *ACS Nano* **2017**, *11*, 9183.
- [86] S. Plimpton, *J. Comput. Phys.* **1995**, *117*, 1.